INTERNATIONAL JOURNAL FOR NUMERICAL METHODS IN FLUIDS
Int. J. Numer. Meth. Fluids 2007; **55**:205–223
Published online 13 February 2007 in Wiley InterScience (www.interscience.wiley.com). DOI: 10.1002/fld.1446

Acoustic upwinding for sub- and super-sonic turbulent channel flow at low Reynolds number

H. C. de Lange*, †

Department of Mechanical Engineering, Technische Universiteit Eindhoven, 5600 MB Eindhoven, The Netherlands

SUMMARY

A recently developed asymmetric implicit fifth-order scheme with acoustic upwinding for the spatial discretization for the characteristic waves is applied to the fully compressible, viscous and non-stationary Navier–Stokes equations for sub- and super-sonic, mildly turbulent, channel flow ($Re_\tau = 360$). For a Mach number of 0.1, results are presented for uniform (32^3, 64^3 and 128^3) and non-uniform (expanding wall-normal, 32^3 and 64^3) grids and compared to the (incompressible) reference solution found in (*J. Fluid. Mech.* 1987; **177**:133–166). The results for uniform grids on 128^3 and 64^3 nodes show high resemblance with the reference solution. Expanding grids are applied on 64^3- and 32^3-node grids. The capability of the proposed technique to solve compressible flow is first demonstrated by increasing the Mach number to 0.3, 0.6 and 0.9 for isentropic flow on the uniform 64^3-grid. Next, the flow speed is increased to $Ma = 2$. The results for the isothermal-wall supersonic flows give very good agreement with known literature results. The velocity field, the temperature and their fluctuations are well resolved. This means that in all presented (sub- and super-sonic) cases, the combination of acoustic upwinding and the asymmetric high-order scheme provides sufficient high wave-number damping and low wave-number accuracy to give numerically stable and accurate results. Copyright © 2007 John Wiley & Sons, Ltd.

Received 18 January 2006; Accepted 29 November 2006

KEY WORDS: acoustic upwinding; subsonic; supersonic; turbulent; channel flow

1. INTRODUCTION

High-speed flows are important in gasturbines, airplanes, etc. Through the development in computing facilities, direct numerical simulations (DNS) and large eddy simulations (LES) of these flows are now accessible. This results in the need for suitable unsteady flow solvers. Traditionally, these simulations are performed using spectral methods. However, over the last decade compact implicit

*Correspondence to: H. C. de Lange, Department of Mechanical Engineering (wh2.126), Technische Universiteit Eindhoven, 5600 MB Eindhoven, The Netherlands.
†E-mail: h.c.d.lange@tue.nl

finite difference methods [1] have been successfully developed. These schemes combine high-order accuracy with spectral-like resolution properties. The originally proposed implicit schemes were symmetric, i.e. central-difference schemes which were employed to the convective as well as the diffusive parts of the Navier–Stokes equations. This meant that they could only be used when the grid-Reynolds number was small enough. For flows at higher Reynolds numbers the non-linear convection term transfers energy from lower to higher wave-numbers. In absence of (or with minor) diffusion, this energy is stored at the highest wave-numbers, which leads to undamped growth of the Nyquist wave.

In e.g. [2–4] asymmetric spatial implicit schemes are proposed to supply high-wave number damping to secure that the solution remains numerically stable on all represented wave-numbers. These schemes use scheme-implicit damping, which acts as a high-order hyperviscosity model. Over the years, numerous artificial viscosity models have already been proposed both for shock- and turbulence-capturing. In the present numerical technique, the stability is obtained by applying upwinding on the acoustic waves. This 'acoustic upwinding' was previously proposed by de Lange [4] and, in combination with the proposed asymmetric schemes, studied in a number of one- and two-dimensional test cases. In the present paper, this combined technique is applied to a mildly turbulent channel flow. It will be shown that using 'acoustic upwinding' with asymmetric implicit schemes leads to accurate numerically stable solutions for this turbulent compressible flow situation for both sub- and super-sonic flows. Ergo, the proposed technique is suitable for both low and high Mach-number flows.

The physical problem treated in this paper has already been studied in previous research. In the well-known article by Kim *et al*. [5] an incompressible-flow solution is given, which is used as a reference for our new method throughout this paper. For the higher Mach-number flows, the solutions presented by Coleman *et al*. in [6] are used. Although the present paper focuses on the applicability of the numerical scheme, it is worthwhile to note that the turbulent channel flow problem still contains features which are under investigation. In recent publications (e.g. [7]) the generation of coherent structures in near-wall turbulence has been ascribed to a streak transient growth mechanism. This process appears to be highly similar to the bypass transition mechanism proposed in e.g. [8]. In both cases streamwise vorticity generates low- and high-speed streaks of streamwise velocity, which in turn is responsible for a secondary instability that generates three-dimensional coherent structures. Furthermore, the heat transfer problem of supersonic flows close to $Ma = 1$ has recently received attention in e.g. [9].

As said, the present paper concentrates on the numerical properties of the proposed code. Therefore, the solutions found for different uniform (32^3, 64^3 and 128^3) and non-uniform (expanding wall-normal, 32^3 and 64^3) grids are compared to [5]. In this comparison, the mean velocity profiles and all components of the Reynolds stress are presented. Furthermore, the effect of the resolution on the flow structures formed is briefly studied. In this case the solutions on different grid are compared to find whether both the streaky mean-stream and the wall-normal vortical structures are well represented.

The paper is organized as follows. First, the numerical methods are clarified in detail. The technique used is based on the local one-dimension inviscid (LODI) relations as presented in [10], extended with the inclusion of viscous dissipation. In these calculations the flow is assumed to be isentropic, i.e. adiabatic walls and negligible influence of entropy generation through dissipation. In the next section the geometry and the computation grids are presented. After this the numerical (time and space) discretization techniques are described. The proposed method is an (three-dimensional) extension of the code introduced in [4, 11]. First, low-Mach number ($Ma = 0.1$) results are presented

DOI: 10.1002/fld

for both uniform and non-uniform grids and compared to [5]. Three different uniform grids are used: a low (32^3), middle (64^3) and high (128^3) resolution grid. For the non-uniform grids the low- and middle-resolution grids are used at two different expansion factors. As a next step, the results for higher subsonic isentropic flow at $Ma = 0.3$, 0.6 and 0.9 are presented on the middle-resolution grid to demonstrate the effect of compressibility on the structure of the generated turbulence. The last step is a step-wise increase of the Mach number to supersonic flow conditions ($Ma = 0.25$, 1 and 2). To this end, the equations are extended to allow for non-isentropic flow. Here, the results are compared to the DNS-simulations in [6]. At the end of the paper the main conclusions are summarized.

2. NUMERICAL METHOD

2.1. Governing equations

The compressible unsteady Navier–Stokes equations are written as a sum of inviscid characteristics combined with viscous stresses and dissipation. This is an extension of the LODI method described in [10], where this formulation is used to define boundary conditions for compressible viscous flows. In the non-conservative formulation this leads to the following set of equations:

$$\frac{\partial \rho}{\partial t} = -\sum_i \left[\frac{\rho}{R_g} \mathbf{L}_2 + \frac{1}{2c^2} (\mathbf{L}_1 + \mathbf{L}_5) \right]_i$$

$$\frac{\partial u_i}{\partial t} = \frac{1}{2\rho c} (\mathbf{L}_1 - \mathbf{L}_5)_i - \mathbf{L}_{3j} - \mathbf{L}_{4k} - \frac{1}{\rho} \frac{\partial \tau_{ij}}{\partial x_j} + F_i$$

$$\frac{\partial s}{\partial t} = -\sum_i \mathbf{L}_{2i} + \frac{R_g}{p} (\nabla \cdot (\lambda \nabla T) + \Phi)$$

where ρ is density, u_i is the velocity in direction i, s is entropy, c is the local speed of sound, τ_{ij} is the ij-component of the stress matrix (τ), Φ is the viscous dissipation. The pressure (p), density (ρ) and entropy s are coupled through a state equation:

$$p = p_0 \left(\frac{\rho}{\rho_0} \right)^{\gamma} \mathrm{e}^{s/C_v}$$

Furthermore, the bodyforce (F_i) has been added to supply the forcing necessary. This force only has a non-zero value for $i = 1$ (in x-direction). Its magnitude determines the displacement thickness of the flow and is chosen such that

$$F_1 = \frac{2}{L_y} \left(\frac{Re_\tau \, v_0}{L_y} \right)^2$$

where Re_τ is set equal to 360, L_y is the channel height and v_0 is the kinematic viscosity ($\equiv \mu/\rho$) in the reference state 0.

DOI: 10.1002/fld

The characteristic waves $\mathbf{L}$ are given by

$$\mathbf{L}_{1i} = (u_i - c)\left(\frac{\partial p}{\partial x_i} - \rho c \frac{\partial u_i}{\partial x_i}\right)$$

$$\mathbf{L}_{2i} = u_i \frac{\partial s}{\partial x_i}$$

$$\mathbf{L}_{3i} = u_i \frac{\partial u_j}{\partial x_i}$$

$$\mathbf{L}_{4i} = u_i \frac{\partial u_k}{\partial x_i}$$

$$\mathbf{L}_{5i} = (u_i + c)\left(\frac{\partial p}{\partial x_i} + \rho c \frac{\partial u_i}{\partial x_i}\right)$$

Here $\mathbf{L}_{1i}$ and $\mathbf{L}_{5i}$ are the acoustic waves in direction i, $\mathbf{L}_{2i}$ the convective transport of entropy, $\mathbf{L}_{3i}$ and $\mathbf{L}_{4i}$ represent the cross-wind convective fluxes.

To these conservation equations two equations need to be added:

$$c^2 = \left(\frac{\partial p}{\partial \rho}\right)_s = \gamma \frac{p}{\rho}$$

$$T = \frac{p}{\rho R_g}$$

where c is the speed of sound, γ is the ratio of specific heats, C_v is the specific heat at constant volume and the index s indicates at constant entropy.

For low-Mach-number flows the dissipation in the entropy equation may be neglected and isentropic ($s = 0$) conditions are assumed. For flows at higher Mach numbers, the influence of dissipation increases and, therefore, the entropy equation needs to be solved. This means that in addition to the convective transport, $\mathbf{L}_{2i}$, the conduction, $(\nabla \cdot (\lambda \nabla T))$ and dissipation (Φ) term need to be solved.

The fluid properties are chosen to resemble airflow: $\rho_0 = 1.2$ (kg/m^3), $T_0 = 300$ (K), $R_g = 287$ (J/kg K), $\gamma = C_p/C_v = 1.4$ (−), $\mu = 1.458 \times 10^{-6} T^{1.5}/(T + 110.4)$ (Ns/m^2). C_p is the specific heat at constant pressure, R_g the specific gas constant, μ the fluid viscosity. The heat-conduction coefficient λ is set by choosing the Prandtl number equal to 0.7.

2.2. Geometry

The geometry is a channel with height L_y equal to $2h$ and periodic boundary conditions in flow and spanwise direction. The length of the channel (L_x) is $4\pi h$. In spanwise direction periodic boundary conditions are used over a width (L_z) of $2\pi h$. As proposed by Poinsot and Lele [10]

DOI: 10.1002/fld

the boundary conditions are imposed separately for the characteristic waves and stresses. The no-slip conditions on top and bottom of the channel lead to $\mathbf{L}_{1i} = \mathbf{L}_{5i}$ and $\mathbf{L}_{5i} = \mathbf{L}_{1i}$, respectively.

The size parameter h is set by the channel Reynolds number:

$$Re \equiv \frac{2U_\infty h}{\nu_0} = 8000$$

using an initial guess of U_∞ defined by $Ma = U_\infty / c_0$.

The first set of simulations are performed at low Mach number. This means that the flow may be supposed to be isentropic (adiabatic and no dissipation). For supersonic-flow calculations dissipation needs to be taken into account. For a streamwise periodic flow with adiabatic walls this would inevitably lead to choking; therefore, the walls for the higher Mach-number calculations have been modelled with an isothermal boundary condition ($T = T_w = T_0$). For the entropy at the wall, this leads to

$$\frac{\partial s}{\partial t} = -\frac{R_g}{\rho}\frac{\partial \rho}{\partial t}$$

In the presented simulations, three different grids are used with $N_x \times N_y \times N_x$ equal to $32 \times 33 \times 32$, $64 \times 65 \times 64$, $128 \times 129 \times 128$. For these uniform grids the values of y^+ of the first point next to the wall are 11, 5.6 and 2.8 (respectively). Expanding grids are used to reduce these values for the low- and middle-resolution grids. In this case the first $((N_y - 1)/2) + 1$-grid-points $y(j)$ are distributed according to an exponentially expanding grid:

$$y(j+1) = \Sigma_{j'=1}^{j+1} \alpha^{j'-1} = y(j) + \alpha^j$$

with $y_1 = 0$ and α the expansion parameter, i.e.

$$\left.\frac{y(j) - y(j-1)}{y(j-1) - y(j-2)}\right|_{j=3,((N_y-1)/2)+1} \equiv \alpha$$

Next, the points are distributed over the bottom halve of the channel (h) using

$$y(j) = h\frac{y(j)}{y((N_y - 1)/2) + 1}$$

Finally, this distributed set of points is mirrored and placed across the top half of the channel.

2.3. Discretization

Asymmetric implicit schemes are used for the discretization of all characteristic waves. Here, the fifth-order $I5(r = 5/9)$ scheme is used, as proposed by de Lange [4]:

$$x_1 f'_{i-1} + f'_i + x_2 f'_{i+1} = \frac{b_1}{2}(f_i - f_{i-2}) + a_1(f_i - f_{i-1}) + a_2(f_{i+1} - f_i) + \frac{b_2}{2}(f_{i+2} - f_i)$$

DOI: 10.1002/fld

with

$$a_1 = \frac{14}{9}\frac{1}{1+r}, \quad a_2 = r a_1$$

$$b_1 = \tfrac{1}{18} - \tfrac{1}{8}(a_2 - a_1), \quad b_2 = \tfrac{1}{9} - b_1$$

$$x_1 = \tfrac{1}{3} - \tfrac{3}{8}(a_2 - a_1), \quad x_2 = \tfrac{2}{3} - x_1$$

and

$$r = \tfrac{5}{9}$$

This scheme is equivalent to the fifth-order scheme proposed by Zhong [2]. For the acoustic fluxes $\mathbf{L}_{1i}$ and $\mathbf{L}_{5i}$ the asymmetry is used as an upwinding scheme along the wave propagation velocity. This 'acoustic upwinding' [4] is similar to the technique proposed by Sesterhenn [3]. For all other (dissipative) fluxes, the sixth-order central scheme [1] is used, which is equivalent to the fifth-order scheme with r chosen equal to 1. No separate scheme for second-order derivatives has been used. The dissipative fluxes are calculated as the derivative of the stress tensor contributions. Therefore, first the stresses are calculated and, next, their derivatives are determined. On both counts the sixth-order scheme is used. For the high Mach-number simulations $\mathbf{L}_2$ [10] also needs to be evaluated. Since, this is a convective flux, it is discretized with the asymmetric fifth-order implicit scheme. Conduction and dissipation are both evaluated using the sixth-order central scheme.

For all discretizations at the non-periodic boundaries (i.e. the walls of the channel) a one-sided third-order implicit scheme is used:

$$f_1' + 2f_2' = \frac{1}{h}\left(2f_2 - 2\frac{1}{2}f_1 + \frac{1}{2}f_3\right)$$

$$f_{N_y}' + 2f_{N_y-1}' = \frac{-1}{h}\left(2f_{N_y-1} - 2\frac{1}{2}f_{N_y} + \frac{1}{2}f_{N_y-2}\right)$$

for the boundary point. For the second point, next to the boundary, (i.e. $j = 2, N_y - 1$) the convective fluxes are calculated with the $I5(r = \frac{5}{9})$ scheme applied with a prescribed (off-the-wall) direction. For the dissipative fluxes in these points the implicit fourth-order Pade scheme is used [1].

In the case of non-equidistant grid (y)-spacing, the same discretization technique is used based on

$$\frac{\partial f}{\partial y} = \frac{\partial j}{\partial y}\frac{\partial f}{\partial j}$$

The derivative of f with respect to j is calculated using the appropriate implicit high-order scheme. For the derivative of y with respect to j the sixth-order implicit scheme is used. Note that for the given expanding grid it is also possible to determine $\partial y/\partial j$ analytically. Simulations have shown that this gives (almost) identical results. In this paper $\partial y/\partial j$ is always determined numerically.

For the time-marching technique, the split-time step integration proposed by de Lange [11] is used. In this split-time integration the integration of each of the fluxes is bound by its own stability criterion, which decreases the calculation time. Furthermore, it is a low-storage method; the explicit time integrations (third-order Runge–Kutta (RK3) [12] on the smallest (acoustic) time

DOI: 10.1002/fld

scale and second-order predictor corrector on the convective and diffusive time-levels) use only one storage variable per time-split level. As said, for the maximum size of the time step for the integration of the different fluxes each has its separate stability limit. As long as these limits are obeyed the solution proofs to be numerically stable:

$$\frac{1}{\Delta t_{\mathrm{d}}} \geqslant \max_{i,j,k} \frac{\nu}{3} \left(\frac{1}{\mathrm{d}x^2} + \frac{1}{\mathrm{d}y^2} + \frac{1}{\mathrm{d}z^2} \right)$$

$$\frac{1}{\Delta t_{\mathrm{c}}} \geqslant \max_{i,j,k} \left(\frac{|u|}{\mathrm{d}x} + \frac{|v|}{\mathrm{d}y} + \frac{|w|}{\mathrm{d}z} \right)$$

$$\frac{1}{\Delta t_{\mathrm{a}}} \geqslant \max_{i,j,k} \left(\frac{|u|+c}{\mathrm{d}x} + \frac{|v|+c}{\mathrm{d}y} + \frac{|w|+c}{\mathrm{d}z} \right)$$

where Δt_{d}, Δt_{c} and Δt_{a} represent the diffusive, convective and acoustic time step, respectively. The $\max_{i,j,k}$ indicates the maximum over all interior grid points and $\mathrm{d}x$, $\mathrm{d}y$ and $\mathrm{d}z$ are the local grid-spacing in x, y and z directions. In the presented calculations, these criteria are always satisfied. Furthermore, it has been checked that in all cases presented the chosen size of the time step has negligible influence on the solutions.

3. RESULTS

In this section the simulation results are presented. To obtain the time-average solutions calculations are first run over long enough time to get steady average profiles. Next, the results are sampled each 0.5 L_x/U_0 time-units during 10 L_x/U_0 time-units. In these samples, all parameter values are first averaged in both the x and z directions, which leads to spatial-averaged cross-channel parameter profiles. Subsequently, these profiles are averaged over all time samples. This averaging procedure is denoted by brackets $\langle\rangle$.

Obviously, the mean velocity in the channel depends on the accuracy to which the solution is able to solve the fluctuating stresses at the wall. Therefore, a first comparison between the different results can be based on the maximum of the average velocity ($\langle u \rangle_{\max}$). The simulation results are then compared to those found in [5], using time-averaged velocity profile ($\langle u \rangle / \langle u \rangle_{\max}$) and the components of Reynolds stresses (R_{ij}) defined by

$$R_{ij} = \frac{\langle u_i' u_j' \rangle}{\langle u \rangle_{\max}^2}$$

where $u_{i,j}'$ denotes the deviation of $u_{i,j}$ from its average value $\langle u_{i,j} \rangle$.

3.1. Uniform grids

The results obtained with the low ($32 \times 33 \times 32$), middle ($64 \times 65 \times 64$) and high ($128 \times 129 \times 128$) resolution grids are now first presented. The mean velocities $\langle u \rangle$ for these grids result in channel Reynolds ($2h\langle u \rangle / \nu_0$) numbers of 9400, 6270 and 6100, respectively. This indicates that the coarsest grid is not sufficient to solve this problem. On the other hand, on the two finer grids the solutions seem to give similar results, since the difference in these Reynolds numbers is in the order of a few percent. To judge the grid convergence-rate of the proposed technique, the results on

DOI: 10.1002/fld

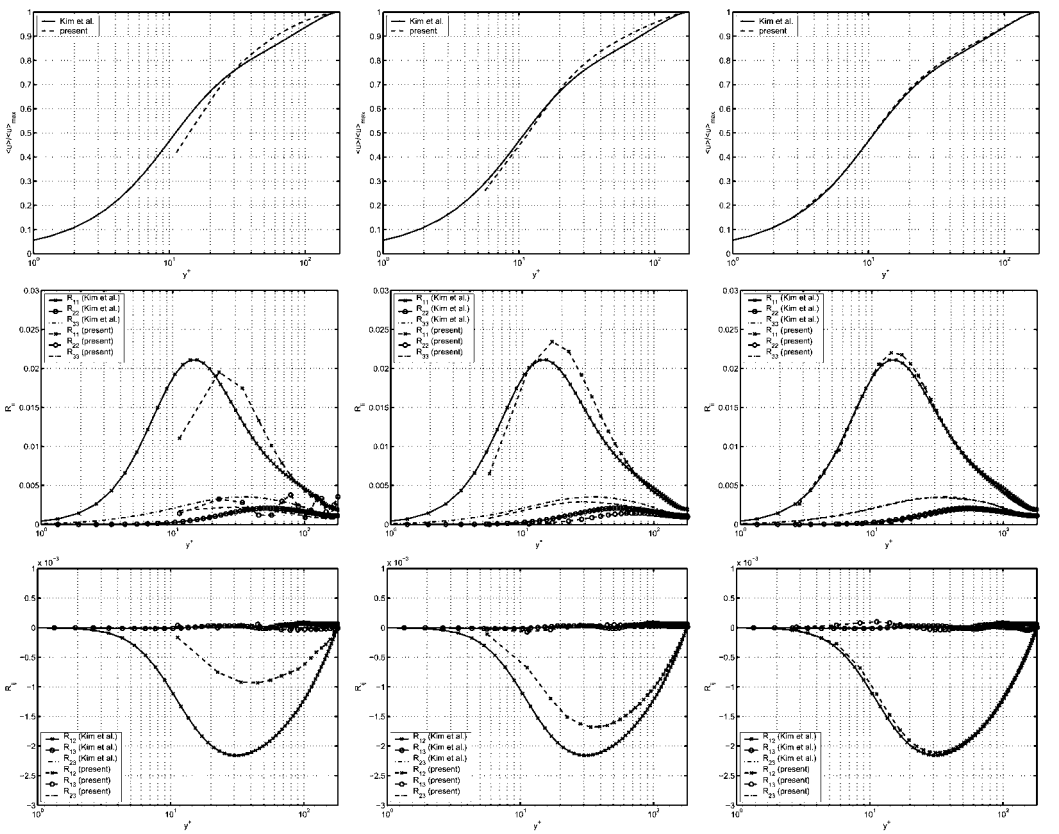

Figure 1. The mean velocity profile (top: $\langle u \rangle / \langle u \rangle_{\max}$), diagonal Reynolds stresses (middle: R_{ii}), off-diagonal Reynolds stresses (middle: R_{ij}) for the uniform low (left), middle (middle) and high (right) resolution grids.

a $48 \times 49 \times 48$ have been added. The channel Reynolds numbers on this grid is about 6700. Based on these numbers, the estimated convergence-rate is of order four.

As the next step, the obtained mean velocity profiles ($\langle u \rangle / \langle u \rangle_{\max}$) are compared to that of [5] (see the top row of Figure 1). The results show that the present results on the high-resolution grid are close to those presented in [5]. More surprisingly, the same still goes for the middle-resolution grid. Although the mean profile near the wall shows a little more deviation, the general shape is still well predicted. For the low-resolution solution this remains true in the global sense. The thickness of the boundary layer is still resolved. However, at this resolution the shape of the profile shows a significant loss of accuracy.

The middle row of Figure 1 gives the three diagonal Reynolds stresses (R_{ii}). The main contribution to R_{ii} is formed by the R_{11}-contribution. Both other terms (R_{22} and R_{33}) are significantly smaller. On the highest resolution, all R_{ii}-contributions are accurately resolved. For R_{22} and R_{33}, the difference between the reference and this solution is hardly visible (they show errors smaller than 3%), while the R_{11} contribution shows a slight deviation at the top which is a little closer to

DOI: 10.1002/fld

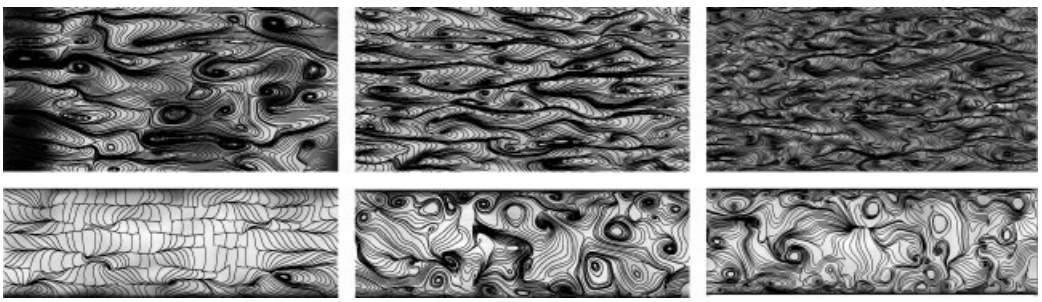

Figure 2. The horizontal (top) and vertical spanwise (bottom) cross-section of the velocity field for the uniform low (left), middle (middle) and high (right) resolution grids.

the wall (at y^+ equal to 14 instead of 14.5) and higher (0.022 instead of 0.021). On the middle resolution, the differences between the reference and the present solution are somewhat larger. The predicted R_{22} and R_{33} now are visibly (about 20%) smaller, while the maximum in R_{11} has increased to 0.023 and shifts away from the wall to y^+ equal to 16. The low-resolution grid is unable to resolve the Reynolds stresses. This results in the oscillatory behaviour of R_{22}. It appears that there exists a (numerical) wall-to-wall wave in v', which has a wavelength of about 5–6 grid-points (ergo of about 60 wall units).

The same trend continues to be true for the non-diagonal Reynolds stresses (R_{ij}). In this case the largest contribution comes from the R_{12}. For the high-resolution grid, this stress term is reproduced accurately. The middle resolution still holds on to the global structure although differences now grow to about 20%. The low-resolution solution still shows the minimum in R_{12}. However, its value is 50% off. The other two, R_{13} and R_{23}, show that there is hardly any correlation in these velocity components. On all grids, this is also found in the present calculations. It is, however, worthwhile to note that calculations need to run over a long enough time to reduce the correlation to small values (in fact the longer they run the smaller R_{13} and R_{23} become).

As the last step in the comparison of these results the instantaneous results for a vertical spanwise and horizontal cross-section of the flow field are presented in Figure 2. In both planes the in-plane (resp. $v-w$ and $u'-w$) velocity components are represented by streamlines, while the grey-scale gives the plane normal velocity (resp. u and v).

The horizontal cross-section (Figure 2 top) shows the velocity field at $h/8$ from the wall. In this plane the flow consists of a low- and high-velocity streaks. On the sides and heads of these streaks vortices appear with a typical size of $h/4$. At the middle-resolution level, the structure can still be predicted. On the low-resolution grid the streaky structure loses a lot of its features. Still globally the main characteristics of the streaks and vortices remain intact.

For the vertical cross-section, the high-resolution result shows the bursts of streamwise vorticity which are responsible for the transport of low-momentum fluid from the wall and high-momentum fluid towards the wall. In this way they cause the velocity streaks which were present in the horizontal cross-section. The typical size of these vortices is about $h/4$. For the middle-resolution grid this same flow structure is found. The size of the vortices can still be resolved. This is no longer true for the low-resolution solution. For this grid the size of the vortices ($h/4$) corresponds to about 4 nodes in wall-normal and 2 nodes in spanwise direction. Obviously, on this grid these structures can no longer be resolved.

DOI: 10.1002/fld

The structures present in this mildly turbulent boundary layer are very similar to the structures found in the study of bypass boundary-layer transition, e.g. [8]. In that case the coupling of streamwise vorticity and velocity streaks is well-established [13]. The secondary instability of these streaks is held responsible for the final breakdown to turbulence. At present the description of this breakdown is studied [14, 15]. One possible explanation is the growth of wall-normal vorticity in the shear layers between streaks. The results in Figure 2 also show this type of structures, i.e. streamwise vorticity coupled to velocity streaks with wall-normal vortices in the shear regions between streaks.

3.2. Spectral properties

The discretization used in these simulations has been chosen to have damping restricted to the highest wave-numbers. As such, the scheme provides an (anisotropic) hyperviscosity term of the order $h^5(\partial^6 u/\partial h^6)$. This high-order implicit asymmetric discretization combined with acoustic upwinding has proved to give satisfactory results in one- and two-dimensional test-problems [4]. Furthermore, similar schemes have also been applied to DNS-calculations of transitional flows [2] and [3]. Similar DNS-channel flow calculations have also been performed in [16]. The major difference with the technique used in [16] is that, due to the use of the acoustic upwinding with the high-order asymmetric scheme, the present calculations can be performed on (very) coarse grids without the necessity of introducing additional damping for either shock-capturing (ENO) or turbulent dissipation from a LES-model.

On each resolution, the scheme must be able to simulate a sustained turbulent sub- and supersonic flow. This means that these simulations test both the accuracy (turbulent production) and the damping ('turbulent dissipation') of the numerical technique. To get an idea of the spectral performance of the code, the span- and stream-wise-mean line-spectra of u at different resolutions are compared in Figure 3. This shows the resemblance between the spectrum found at the 64^3-grid compared to that of the 128^3-grid. The 32^3-grid shows a slightly distorted spectrum. As already shown, the results on this resolution lead to vortex-rolls in the boundary layer. Therefore, the turbulent structures in this case has not been accurately predicted. For completeness, the spectrum on the 48^3-grid is added. On all presented grids the dissipation at the smallest grid scale has a comparable effect. This means that all spectra have similar shapes and, only for wave-numbers close to about 2–3 times the Nyquist wavelength, the numerical dissipation starts to reduce the kinetic energy.

The essential feature of the presented spectra is that, on all resolutions, the damping provided by the numerical scheme leads to very similar decaying spectral-energy. Therefore, an increase of resolution leads to more resolved scales (as one would expect). And, more important, the decay towards the non-resolved scales is (almost) independent of the chosen resolution.

3.3. Expanding grids

The accuracy of the results for the low- ($32 \times 33 \times 32$) and middle- ($64 \times 65 \times 64$) resolution grids can be increased by applying expanding grids. For the low-resolution grid, an expansion factor (α) of 1.1 is used. On this grid the y^+ on the first point next to the wall equals 5. Note that, in reference to the uniform grids, this means that this grid is close to the middle-resolution grid. Similarly, the expansion factor on the middle resolution is chosen to be $\alpha = 1.05$, which results in y^+ values of 2.4. It is worthwhile to note here that calculations for higher expansion factors lead to similar results, i.e. increase of the expansion factor did not increase the accuracy. This may

DOI: 10.1002/fld

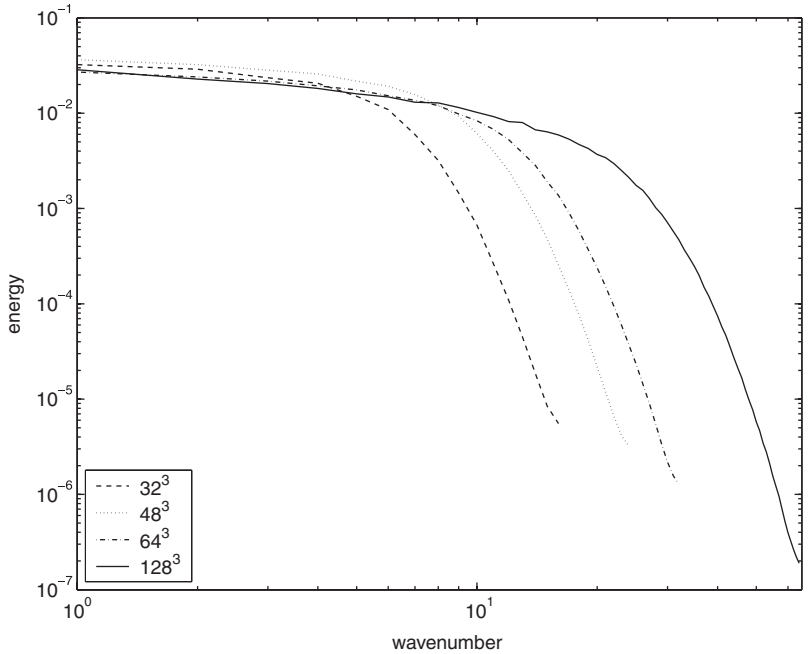

Figure 3. The span- and stream-wise mean line-spectra of u for $Ma = 0.1$ on the channel centre-plane for four different uniform grids.

indicate that through the redistribution of accuracy, the error remains more or less similar, i.e. the accuracy depends mainly on the total number of points and less on their distribution.

The profiles of $\langle u \rangle / \langle u \rangle_{\max}$, R_{ii} and R_{ij} are presented in Figure 4 for the low resolution (left) and for the middle resolution (right). The low-resolution grid results show an improved solution. The maximum value and position of R_{11} are reproduced with an accuracy comparable to that of the middle-resolution (uniform) grid. On the other hand, the minimum in R_{12} hardly seems to have shifted. Furthermore, although greatly improved (no longer oscillatory), R_{22} and R_{33} are still far from accurate. The increased resolution close to the wall increases the accuracy to which the wall stress can be resolved. However, this leads to a decrease of the accuracy of the resolved scales in the channel centre.

The improvement of the representation of the flow structures becomes obvious from the cross sections of the flow, presented in Figure 5. The vortical and streaky structures appear to be reasonably well captured. This indicates that resolving the flow structures in wall-normal direction is crucial.

For the middle-resolution expanding grid, only minor changes in all profiles are detected. Obviously, in the expanding grid the improvement of resolution close to the wall is paid for by the reduction of accuracy in the remainder of the domain. And it appears that for all variables presented the costs never exceed the gain. This results in the increased accuracy of $\langle u \rangle / \langle u \rangle_{\max}$ and R_{11} close to the wall, while there is no improvement in e.g. R_{12} and the maximum value of R_{11} is further off.

DOI: 10.1002/fld

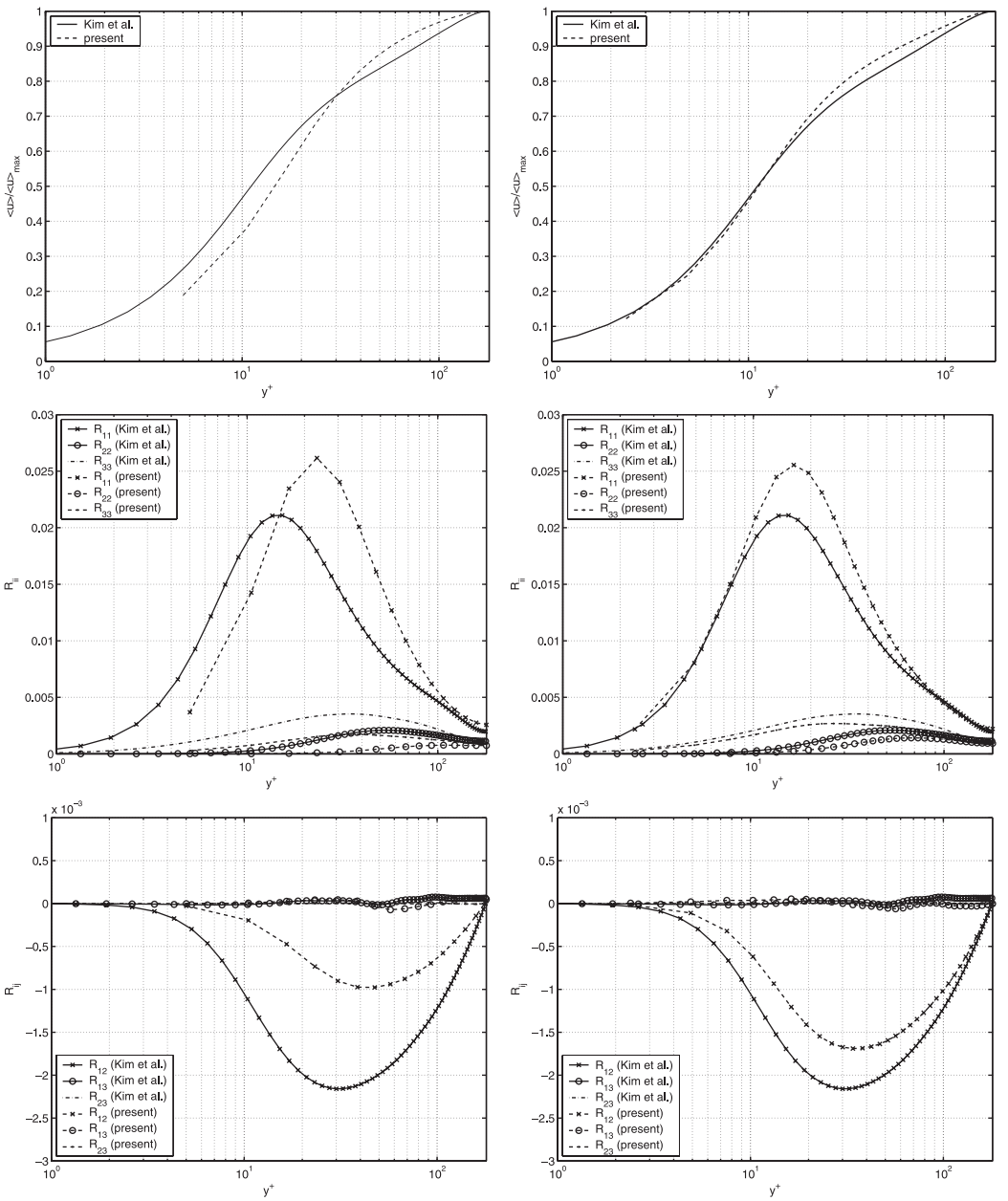

Figure 4. The mean velocity profile (top: $\langle u \rangle / \langle u \rangle_{\max}$), diagonal Reynolds stresses (middle: R_{ii}), off-diagonal Reynolds stresses (bottom: R_{ij}) for the expanding grids of low resolution with $\alpha = 1.1$ (left) and middle resolution with $\alpha = 1.05$ (right).

DOI: 10.1002/fld

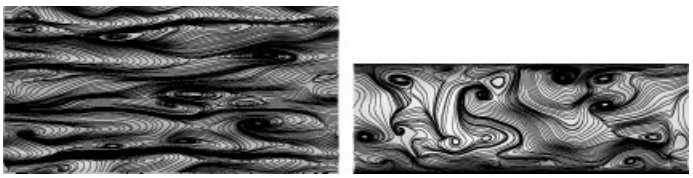

Figure 5. The horizontal (left) and vertical spanwise (right) cross-section of the velocity field for the expanding grids of low resolution with $\alpha = 1.1$.

To appreciate the accuracy obtained on the uniform grids, it is worthwhile to note that the use of expansion factors comes at the cost of an increase in computational effort. This is due to the increase of the amount of time-steps needed to assure numerically stable solutions. The smallest time-step (Δt_a, for the acoustic integration) scales linearly with the size of the grid. This means that the time needed for $\alpha = 1.05$-grid on the middle resolution takes about 3 times ($y^+_{\text{unif}}/y^+_{\text{exp}}$) longer. On the other hand, one might also judge the results on the low-resolution grid with an expansion factor of 1.1 to be sufficiently accurate. When comparing the computational effort on this grid to that of the uniform middle-resolution grid the number of nodes is obviously decisive. This means that the necessary time for the calculations on the low-resolution expansion grids is about 8 times less.

3.4. Subsonic isentropic flow

One advantage of the proposed numerical scheme is that it is suitable for compressible flow simulations. This means that the effect of compressibility on the turbulent structures can be examined by increasing the Mach number. Note, however, that the isentropic modelling only suffices for lower Mach numbers. If the presented technique should be extended to higher Mach numbers, the entropy equation must be taken into account. This also means that the wall boundary conditions need to be extended (isothermal or adiabatic). For lower Mach numbers the isentropy assumption remains valid. The results obtained at $Ma = 0.3, 0.6$ and 0.9 are calculated on the uniform 64^3-grid. In all cases the proposed numerical scheme leads to stable results, due to the used acoustic upwinding, which acts as a low-pass filter on the characteristics. Since the results for these Mach numbers give highly similar results, only those on $Ma = 0.6$ are presented in detail.

As Figure 6 shows the mean velocity profile is barely influenced. Apparently, the mean velocities tend to concentrate a little more on the channel centre, which results in a slight decrease in the velocity near the walls. The increased Mach number results in a shift of the peak in R_{11} towards the wall. For $Ma = 0.6$, the peak is found at $y^+ \approx 15$. The profiles also show that the peak value of R_{11} increases. The increased Mach number leads to an increase of R_{22}. This must mean that the energy of v-fluctuations must have increased. This effect of the change in Mach number also leads to an increase in R_{12}. This similarity in the low-Mach regime corresponds to subsonic results, presented in e.g. [6]. This is a clear indication that the proposed numerical technique accurately solves the subsonic channel flow.

Comparison of the flow structures obtained at $Ma = 0.6$ (see Figure 7) to those at $Ma = 0.1$ (Figure 2) shows that the influence of compressibility on the dominating flow structures is not evident. It appears that, in the horizontal (streamwise) cross-section the velocity streaks become shorter as the Mach number is increased. Furthermore, the wall-normal vortices formed in the shear within streaks appear to be somewhat condensed. In the vertical (spanwise) cross-section

DOI: 10.1002/fld

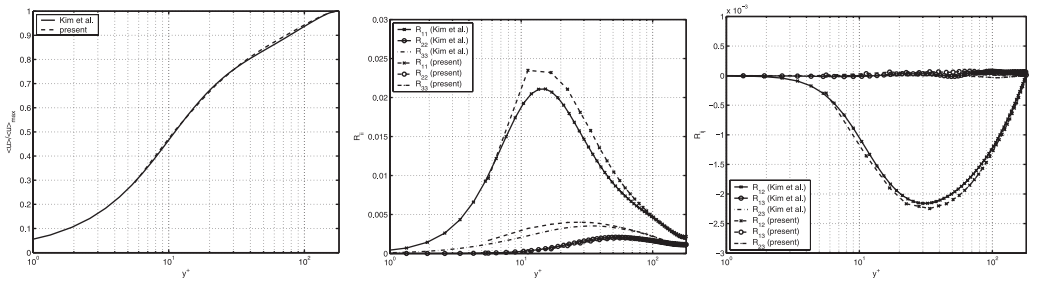

Figure 6. The mean velocity profile (right: $\langle u\rangle/\langle u\rangle_{\max}$), diagonal Reynolds stresses (middle: R_{ii}), off-diagonal Reynolds stresses (left: R_{ij}) for $Ma = 0.6$.

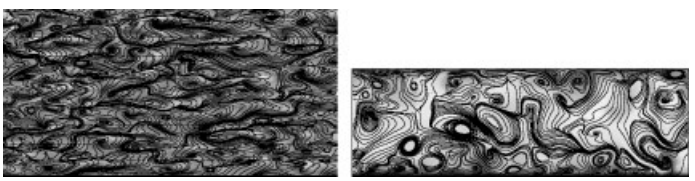

Figure 7. The horizontal (left) and vertical spanwise (right) cross-section of the flow for $Ma = 0.6$.

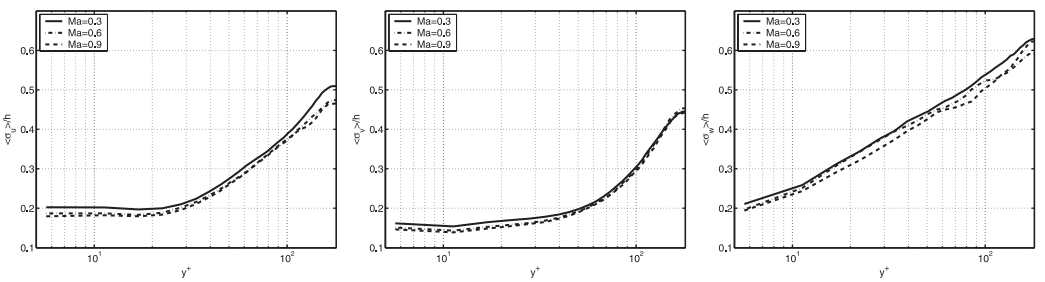

Figure 8. The streamwise- and time-mean peak width of the spanwise autocorrelation $[h]$ for u (left), v (middle) and w (right) for $Ma = 0.3$, 0.6 and 0.9.

one would expect to recognize the result of the increase in v-fluctuations. However, the results in these cross-sections show to be very similar; the increase in R_{22} and the peak-shift towards the wall are too small to be noticeable in the flow patterns.

A quantitative estimate of the size of the flow patterns can be determined from the peak width of the spanwise autocorrelation of the three velocity components (σ_u, σ_v, σ_w). This peak width is averaged in streamwise direction and for all time steps (this averaging is again denoted with brackets $\langle\rangle$). The mean wall-normal size distributions for the three simulated Mach numbers are presented in Figure 8. First, it is worth noting that the estimated structure size close to the wall is about $h/5$, which closely agrees with previous estimations based on the flow patterns. A second observation is that the structures-size development at different heights for u and v is very similar,

DOI: 10.1002/fld

while that of w shows different behaviour. Close to the wall $\langle\sigma_u\rangle/h$ is about 0.2 and from y^+ of 20 on $\langle\sigma_u\rangle/h$ rapidly increases to about 0.5. The same holds for $\langle\sigma_v\rangle/h$; however, the size of these structures is slightly smaller and the increase starts somewhat later. The scales represented by $\langle\sigma_w\rangle/h$ are larger; they grow from 0.2 at the wall to 0.6 in the channel centre. Furthermore, they appear to grow exponentially with y^+. Figure 8 shows that the introduction of compressibility leads to a decrease in the size of the flow patterns. For both $\langle\sigma_u\rangle/h$ and $\langle\sigma_w\rangle/h$, the scale size throughout the channel decreases in the order of 10%. For $\langle\sigma_v\rangle/h$ the influence of the Mach number is somewhat smaller and confined to the near-wall region.

3.5. *Supersonic flow*

The Mach number is now stepwise increased from 0.25, 1 to 2, similar to the DNS-results in [6], to test if the hyperviscosity provided in the proposed technique can also be applied to flows at supersonic speeds. As already mentioned, the equations are now extended with the entropy equation, taking the conduction and dissipation into account and using isothermal wall conditions.

In Figure 9 the results for $Ma=2$ are presented on the middle-resolution grid. These figures show that even at supersonic Mach numbers the main flow-features remain to be very similar. There are, however, a couple of noteworthy changes. The inward shift of the maximum of R_{11} has reversed. It is now found at $y^+\approx 22$. Furthermore, the strength of both R_{22} and R_{33} has gone down. The outward shift of the u-fluctuations combined with the decreased level of v-fluctuations also shows in the shifted and decreased levels of R_{12}.

The structure of the turbulent fluctuations may be evaluated from the mixing length and Reynolds-stress correlation. These are shown in Figure 10 for the different grids at $Ma=2$. The solutions on all three resolutions show a very good resemblance to the plots presented in [6] which again validates the present numerical technique.

In Figure 11 the profiles of the mean temperature ($\langle\theta\rangle$) and temperature fluctuations ($\langle\theta'\rangle_{\mathrm{rms}}$) are shown, scaled according to

$$\theta \equiv \frac{T - T_w}{\langle u\rangle^2_{\max,y}/(2C_{\mathrm{p}})}$$

The result shows that the scaled-temperature profiles look very similar for increasing Mach numbers, while the maximum temperature level shifts from approximately 0.5 to 0.55.

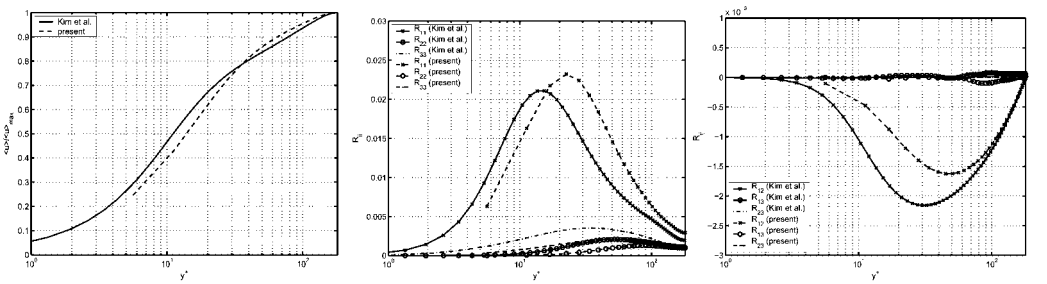

Figure 9. The mean velocity profile (right: $\langle u\rangle/\langle u\rangle_{\max}$), diagonal Reynolds stresses (middle: R_{ii}), off-diagonal Reynolds stresses (left: R_{ij}) for $Ma=2$.

DOI: 10.1002/fld

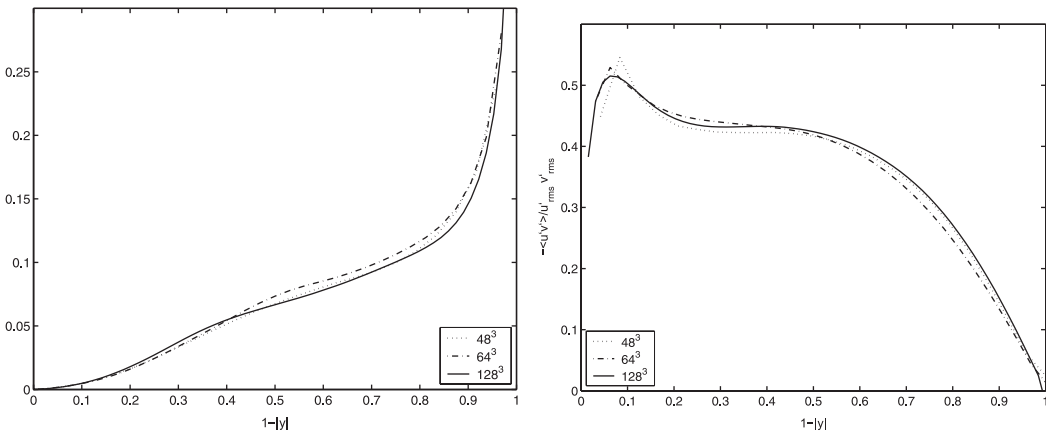

Figure 10. The mean mixing length (left) and Reynolds-stress correlation (right) for $Ma = 2$ for the three different resolutions.

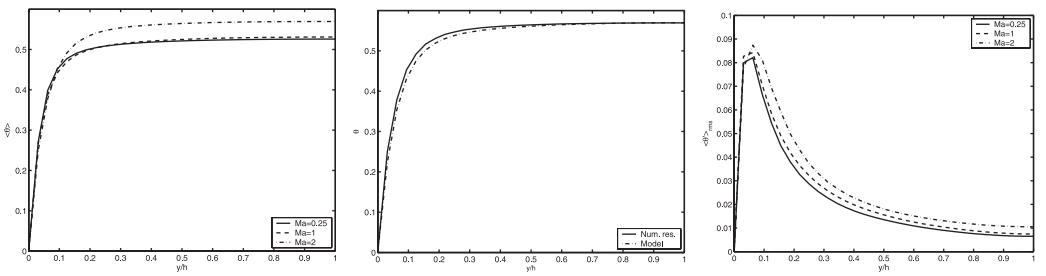

Figure 11. The mean temperature profile (left: θ), for $Ma = 2$ compared to the model equation (middle) and the temperature fluctuations (right: $\langle \partial\theta \rangle_{\mathrm{rms}}$) for $Ma = 0.25$, 1 and 2.

In Figure 11 (middle) the $Ma = 2$ result is compared to the model equation [9]:

$$\langle T_{\mathrm{model}} \rangle = T_w + \langle u \rangle \left[\frac{\partial \langle T \rangle / \partial y}{\partial \langle u \rangle / \partial y} \right]_w - Pr_t \frac{\langle u \rangle^2}{2C_{\mathrm{p}}}$$

The numerical result shows very close resemblance with the model for $Pr_t \approx 0.5$. For smaller Mach numbers the similarity to the model also holds with a slight decrease of Pr_t (to about 0.45 at $Ma = 0.25$). The temperature-fluctuation profiles in Figure 11 (right) are scaled in a similar way. The maximum close to the wall shifts outward with increasing Mach number, from about $y/h = 0.04$ for $Ma = 0.25$ to about $y/h = 0.06$ for $Ma = 2$. These results closely resemble the results in [6].

One of the main effects of the increased Mach numbers noted in [6] is the increased coherence of the velocity streaks. In Figure 12 this effect is also clearly noticeable. The flow structures for $Ma = 0.25$ still resemble the structure as it was presented in Figure 2. The change of the boundary condition or the slight increase of the Mach number compared to those figures do not show in the flow structure. However, at the $Ma = 2$ the velocity streaks have indeed grown more coherent. The number of side-branches and their effect on the streaks have decreased.

DOI: 10.1002/fld

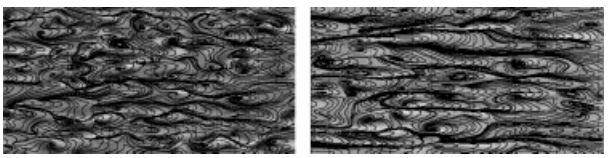

Figure 12. The horizontal cross-section at $y+ \approx 0.04$ of the flow for $Ma = 0.25$ (left) and 2 (right).

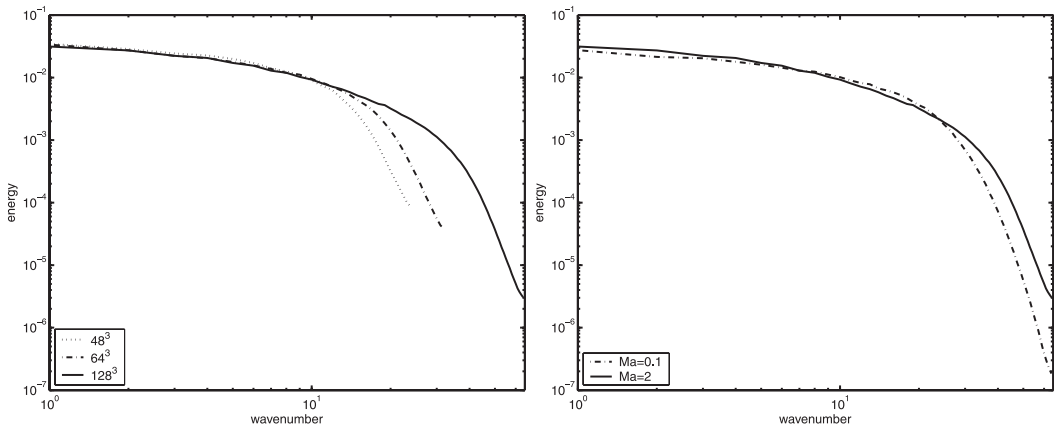

Figure 13. The span- and stream-wise mean line-spectra of u on the channel centre-plane for different resolutions and $Ma = 2$ (left) and comparing $Ma = 0.1$ and 2 on the 128^3-grid (right).

These results show that the proposed numerical technique leads to stable and accurate results on the 64^3-grid. The spectral properties of the solutions for different resolutions (48^3-, 64^3- and 128^3-grids) are compared in Figure 13 (left). The spectra show that, for the supersonic flow, the resemblance of the spectra on different resolutions remains intact. Also in these cases, the proposed technique provides damping retained to high wave-numbers, while it still accurately resolves the lower wave-numbers. In Figure 13 (right) the spectra for different Mach numbers ($Ma = 0.1$ and 2) are compared for the high-resolution grid. The difference between the spectra is a shift of the energy from the mid-range to the lower wave-numbers for the higher Mach number. This is consistent with the notion of the increased streamwise coherence of the streaks. Furthermore, the damping (from 2 times the Nyquist wave) in the subsonic case seems to be more effective, leading to an increase of the energy on the grid-scale for the $Ma = 2$ result.

4. CONCLUSIONS

The described numerical procedure is based on the viscous extension of the LODI-formulation of the compressible flow equations presented in [10]. The steady mean conditions of the flow in the turbulent channel are induced by adding a constant force term to the momentum equation in the main stream flow direction. The magnitude of this force term determines Re_τ of the flow, which is set at 360. Furthermore, (since the flow is compressible) the Mach number has to be set. In the

DOI: 10.1002/fld

first calculations it is fixed at 0.1. For the time-discretization a split-time integration is used [11] in which the diffusive, convective and acoustic fluxes are separated and solved each on their separate time steps. For the spatial discretization of the convective fluxes an asymmetric implicit scheme is combined with acoustic upwinding as proposed in [4]. The viscous stresses are calculated using sixth-order implicit discretization as proposed in [1].

The numerical scheme is applied to the flow on three different resolution (low: 32^3, middle: 64^3 and high: 128^3) uniform grids. For the low- and middle-resolution grid a non-uniform (wall-normal expanding) grid is also applied. For all grids investigated, the code leads to numerically stable solutions, as long as the CFL criteria on the three different time step levels are satisfied. The solution on the high-resolution grid agrees closely with the reference solution of [5]. The mean velocity profile as well as the contributions to the Reynolds stresses are all accurately resolved. The results on the middle-resolution are still close to the reference solution, although the differences become noticeable. On the low-resolution grid the mean velocity profile still appears to be more or less accurate. However, on this resolution the vortex-bursts cannot be resolved. For the expanding low-resolution grid the spanwise cross-sections of the flow do show the expected vortex bursts. The results show that expanded grids increase the accuracy of the solutions; however, the gain appears limited.

The spectra of the solutions of different grids show that the damping imposed by the proposed technique is restricted to about 2–3 times the Nyquist wavelength. Furthermore, the spectra on the different resolutions show a high degree of similarity towards the non-resolved scales. This means that the provided damping scales very well with the resolved scales.

To show the applicability of the proposed numerical technique to higher (subsonic/isentropic) Mach numbers, the results for a stepwise increase of the Mach number form 0.1 to 0.9 are explored. The increase of the Mach number results in a slight increase of R_{11} and R_{12}. The main features of the flow are independent of the Mach number; in all cases the flow pattern shows the velocity streaks with local wall-normal vortices. The velocity streaks at higher Mach numbers appear to become somewhat shorter with more condensed wall-normal vortices. An evaluation of the width of the autocorrelation peak shows that the size of the structures is indeed (about 10%) smaller for the larger Mach numbers.

As a last step, the Mach number is increased to 2 for isothermal channel-walls. The mean temperature and temperature fluctuation profiles show a very good resemblance to those in [6], this also holds for the mixing length and the correlation of Reynolds stress. The simulations on all three resolutions give very satisfactory results. Furthermore, spectral analysis shows that, just as in the subsonic case, the numerical damping is restricted to 2–3 times the Nyquist wavelength and the spectral similarity on the different resolutions remains valid.

These results show that the proposed numerical technique (the combination of acoustic upwinding with high-order asymmetric implicit discretization) leads to stable and accurate results for sub- and super-sonic turbulent flows validated by a comparison to the DNS-results in [5, 6]. In the studied cases, the selective high-wave number damping applied to the non-linear characteristics replaces both turbulent dissipation models as well as shock-capturing schemes and makes the proposed technique suitable for both sub- and super-sonic turbulent flows.

REFERENCES

1. Lele SK. Compact finite difference schemes with spectral-like resolution. *Journal of Computational Physics* 1992; **103**:16–42.
2. Zhong X. High-order finite-difference schemes for numerical simulation of hypersonic boundary layer transition. *Journal of Computational Physics* 1998; **144**:662–709.

DOI: 10.1002/fld

3. Sesterhenn J. A characteristic-type formulation of the Navier–Stokes equations for high-order upwind schemes. *Computers and Fluids* 2001; **30**:37–67.
4. de Lange HC. Inviscid flow modelling using asymmetric implicit finite difference schemes. *International Journal for Numerical Methods in Fluids* 2005; **49**:1033–1051.
5. Kim J, Moin P, Moser R. Turbulence statistics in fully developed channel flow at low Reynolds number. *Journal of Fluid Mechanics* 1987; **177**:133–166.
6. Coleman GN, Kim J, Moser RD. A numerical study of turbulent supersonic isothermal-wall channel flow. *Journal of Fluid Mechanics* 1995; **305**:159–183.
7. Schoppa W, Hussain F. Coherent structure generation in near-wall turbulence. *Journal of Fluid Mechanics* 2002; **453**:57–108.
8. Brandt L, Cossu C, Chomaz J-M, Huerre P, Henningson DS. On the convective unstable nature of optimal streaks in boundary layers. *Journal of Fluid Mechanics* 2003; **485**:221–242.
9. Morinishi Y, Tamano S, Nakabayashi K. Direct numerical simulation of compressible turbulent channel flow between adiabatic and isothermal walls. *Journal of Fluid Mechanics* 2004; **502**:273–308.
10. Poinsot TJ, Lele SK. Boundary conditions for direct simulations of compressible viscous flows. *Journal of Computational Physics* 1992; **101**:104–129.
11. de Lange HC. Split time-integration for low-Mach number compressible flows. *Communications in Numerical Methods in Engineering* 2004; **20**(7):501–509.
12. Kennedy CA, Carpenter MH, Lewis RM. Low-storage, explicit Runge–Kutta schemes for compressible Navier–Stokes equations. *Applied Numerical Mathematics* 2000; **35**:177–219.
13. Andersson P, Brandt L, Bottaro A, Henningson DS. On the breakdown of boundary layer streaks. *Journal of Fluid Mechanics* 2001; **428**:29–60.
14. Hoeffner J, Brandt L, Henningson DS. Transient growth on boundary layer streaks. *Journal of Fluid Mechanics* 2005; **537**:91–100.
15. Mans J, Kadijk E, de Lange HC, van Steenhoven AA. Breakdown in a boundary layer exposed to free-stream turbulence. *Experiments in Fluids* 2005; **39**(6):1071–1083.
16. Lechner R, Sesterhenn J, Friedrich R. Turbulent supersonic channel flow. *Journal of Turbulence* 2001; **2**:001.

DOI: 10.1002/fld